Journal of Applied Physics ARTICLE scitation.org/journal/jap

Effects of transmission line geometry on traveling-wave metal-insulator-metal rectenna infrared detectors

Cite as: J. Appl. Phys. **126**, 064503 (2019); doi: 10.1063/1.5083154
Submitted: 28 November 2018 · Accepted: 15 July 2019 ·
Published Online: 9 August 2019

B. Pelz,[1] M. Armanious,[2] and G. Moddel[1,a)]

AFFILIATIONS

[1]Department of Electrical, Computer, and Energy Engineering, University of Colorado, Boulder, Colorado 80309, USA
[2]Redwave Energy Inc., Boulder, Colorado 80301, USA

Note: This paper is part of the Special Topic section "Advances in Terahertz Solid-State Physics and Devices," published in J. Appl. Phys. **125**(15) (2019).

[a)]**Electronic mail:** moddel@colorado.edu

ABSTRACT

The transmission line impedance of traveling-wave diodes can circumvent resistance-capacitance time constant limitations of metal-insulator-metal diodes in rectennas operating at optical frequencies. We performed three-dimensional simulations of a traveling-wave diode rectenna using a linear finite-element electromagnetic solver. We develop a method to analyze metal-insulator-metal traveling-wave rectennas by using the field profiles from the linear finite-element solver and accounting for the nonlinear current-voltage characteristics during postprocessing. The traveling-wave diode length produces resonance at half surface plasmon wavelength intervals. With optimized cross section and length parameters, we observe a peak system responsivity of 239 μA/W and a detectivity of 5.7×10^4 Jones.

I. INTRODUCTION

A rectenna is an antenna coupled to a diode. The antenna absorbs an electromagnetic wave and the diode rectifies the signal to give a DC output. Rectennas were first demonstrated at microwave frequencies by Brown in the 1960s.[1,2] Optical rectennas were first proposed in the 1970s by Bailey.[3] While microwave rectennas can make use of semiconductor diodes and can operate at power conversion efficiencies up to 90%,[4] optical rectennas require an ultrafast diode to operate in the terahertz region. Semiconductor diodes are limited by plasma frequency and electron mobility. For this reason, metal-insulator-metal (MIM) diodes, which use femtosecond fast electron tunneling for rectification, are an excellent candidate.[5–9] However, a fast rectification mechanism is not the only requirement. For efficient AC-to-DC conversion, a good impedance match between the antenna and the diode is required to maximize transferred power and ensure a low resistance-capacitance (RC) time constant.[10,11] Given the inherently capacitive structure of an MIM diode and the trade-off between resistance and capacitance with area, the fundamental cutoff frequency of a lumped-element MIM diode is in the low terahertz, that is,

$$f_{cutoff} = \frac{1}{2\pi RC}. \quad (1)$$

One proposed solution to overcome the RC time constant limitation is the traveling-wave diode (TWD).[12] In such a configuration, the antenna excites a surface plasmon wave that travels down the MIM transmission line. As the wave propagates, it is rectified by the MIM diode. Since the antenna is now loaded by a rectifying transmission line, the impedance seen by the antenna is the input impedance of the line, rather than the capacitive lumped-element MIM impedance. The TWD optical rectenna concept has been demonstrated experimentally in a waveguide-coupled configuration at 1.6 μm[13] and a free-space illumination at 10.6 μm.[14] Previously, the finite-element method (FEM) was used to examine the effects of the cross-section geometry on the TWD rectenna performance with the assumption that the TWD length is much longer than the plasmonic decay length.[15–17] In these cases, the nonlinear characteristic of the MIM junction cannot be included in the finite-element analysis. In other work, the nonlinear

current-voltage [$I(V)$] characteristic was included in a finite-difference time domain (FDTD) simulation examining a TWD for pulse detection.[18] In this work, we focus on the effect TWD length has on the overall performance of the rectenna system using the COMSOL RF module finite element solver.

II. TRAVELING-WAVE STRUCTURE

A TWD differs from a lumped-element rectenna primarily in the method it is fed from the antenna. In a lumped-element configuration, the diode is located at the feed-point of the antenna, where it receives a voltage signal uniformly across the diode as the signal from each antenna leaf enters from opposite sides of the diode. A TWD, on the other hand, requires a transition at the feed-point of the antenna so that the signal from the antenna can couple to the MIM transmission line. This transition excites a surface plasmon mode at the MIM interface. In this way, the power from each antenna leaf propagates in the same direction away from the antenna feed-point and along the TWD. We discuss coupled surface plasmon modes in detail in Sec. IV.

Figure 1 shows an implementation of TWD rectenna with a bowtie antenna, which is similar to the experimental device (but with a simplified geometry) from our previous work.[14] This experimental device was fabricated on a silicon substrate coated with a 300 nm thick layer of silicon dioxide. The space above the device is air. Coherent, plane-wave, 10.6 μm radiation illuminates the device from the top xz-boundary, port 1, on the air side of the antenna. The vertical boundaries (xy and zy) are periodic (effectively a two-dimensional array) on a $10 \times 14\,\mu m^2$ pitch in the x and z directions, respectively. This maintains the plane-wave nature of the illumination and provides a slight boost to antenna performance over nonperiodic boundary conditions. The illumination is polarized along the x-direction, in line with the antenna axis, for maximum absorption. The antenna length, L_{ant}, is 5.2 μm, and the antenna flare angle, θ_{ant}, is 42.5°. We consider the transition at the feed-point to be part of the antenna for the discussion of impedance matching between the antenna and the TWD. This transition uses 250 nm wide metal traces that make 90° turns about a rotation point of 250 nm from the edge of the trace. We use a gold bowtie antenna and hold the geometry constant.

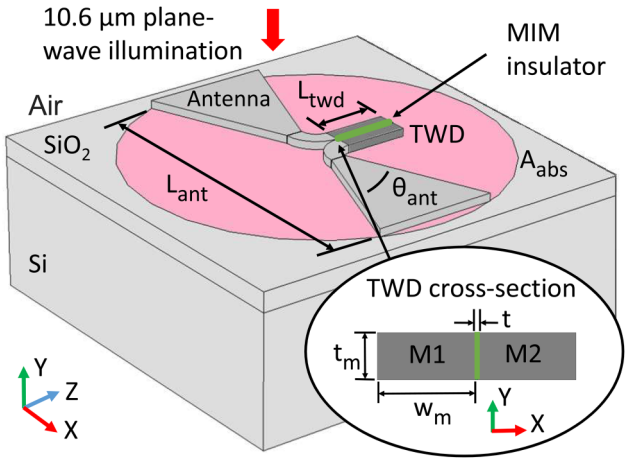

FIG. 1. Illustration of TWD rectenna geometry and illumination conditions. The TWD is the dark gray part of the rectenna structure; the antenna is the light gray part. From each leaf of the antenna, a curved trace extends. These two curved regions are the transition region, which is considered to be part of the antenna.

To understand the effects of the TWD dimensions, we varied the TWD length, L_{twd}, from 300 nm to 2 μm. We also explored the effect of the metal thickness, t_m (60 nm, 120 nm, and 240 nm), which is effectively the transmission line width because the diode is formed on the edge. Finally, we explored a small range of insulator thickness, t (2.5 nm and 5 nm). While changes in t have some effects on the TWD transmission line characteristics, the diode $I(V)$ characteristics are extremely sensitive to changes in the insulator thickness. Because of this sensitivity, t is chosen primarily to achieve the desired $I(V)$ characteristics, namely, low resistance and high asymmetry. The nonlinear and asymmetric characteristic of an MIM $I(V)$ curve arises from the nature of electron tunneling. For practical, low-resistance, MIM diodes, the diode total insulator thickness must be between 2 and 6 nm because of the exponential dependence of tunneling current on insulator thickness.[7,19] When the MIM insulators are too thin, the diode responsivity drops below 0.1 A/W. When the MIM insulators are too thick, the resistance becomes too high (>20 kΩ). Despite the sensitivity of the $I(V)$ curve to insulator thickness, we use the same $I(V)$ model for both insulator thicknesses. This allows us to isolate the effect of insulator thickness on the plasmonic properties of the TWD, by excluding effects from changes in the $I(V)$ characteristics.

The metal trace width of the TWD, w_m, is held at a constant value of 250 nm. We estimate the skin depth of our metals at 28 THz to be between 50 and 100 nm. Since the trace width is larger than the metal skin depth, the plasmonic prorogation will be in part limited by the skin depth. This effect is included directly through the values of the dielectric constants of the metals.

For these simulations, we use a double-insulator MIM diode to take advantage of enhanced asymmetry and responsivity compared to a single insulator.[19,20] Our analysis suggests that tunneling is the dominant conduction mechanism, but we cannot rule out additional charge trapping effects.[21,22] An analysis is available in the supplementary material. The diode $I(V)$ curve is based on an experimentally measured $Ni - NiO(3\,nm) - Nb_2O_5(2\,nm) - CrAu$ diode similar to the experimentally measured TWD.[14] The $I(V)$ data are fit with the exponential model,[23] described by the following two equations:

$$I(V) = I_0(e^{bV_D(\alpha,R_s,V)} - e^{dV_D(\alpha,R_s,V)}), \tag{2}$$

$$V_D(\alpha, R_s, V) = V - I(V)(R_s + \alpha V^2), \tag{3}$$

where V_D is the voltage on the exponential characteristic of the diode and V is the voltage on the series combination of the exponential part of the diode and its series resistance. I is the diode current, and the remaining variables (I_0, b, d, α, and R_s) are the fit coefficients. The fit parameters for the $I(V)$ curve used for this work are as follows: $b = 9.30\,V^{-1}$, $d = 8.31\,V^{-1}$, $I_0 = 1.51 \times 10^{-4}$ A, $\alpha = 320\,\frac{\Omega}{V^2}$, and $R_s = 0\,\Omega$.

To estimate the input power, P_{in}, we approximate the antenna absorption area, A_{abs}, to be the circle that circumscribes the antenna. By choosing the largest possible physical area of the antenna, we are conservative in our estimate of the power available for rectification. Therefore, P_{in} is simply the product of A_{abs} ($24\,\mu m^2$) and illumination intensity, I ($10^5\,W/m^2$, based on our measurement system). Because the illumination is coming from the low-index side of the antenna, the antenna directivity is poor in the direction of illumination,[24] and the maximum absorption is limited to ~13%. This was estimated by removing the TWD portion of the model and replacing it with a lumped-port load that was conjugate matched to the antenna impedance. With the perfectly matched load, the absorption is the maximum absorption possible for that antenna/substrate combination. While the free-space-to-antenna coupling is relatively poor, it is sufficiently absorptive to provide the plasmonic excitation to explore the effects of TWD dimensions on rectenna performance. Therefore, even though the antenna optimization is important for efficient overall rectenna operation, it remains outside the scope of this work.

In the electromagnetic (EM) model, the two insulators are combined into a single insulator with the total combined thickness, t, and an average effective relative permittivity. We use $\epsilon_r = 8.5$ for NiO and $\epsilon_r = 20$ for Nb_2O_5, which are between values found in the literature and our measured values.[13,25,26] When exploring variations in the insulator thickness, a constant thickness ratio of 2:3 for Nb_2O_5 to NiO is maintained, giving an effective relative permittivity, $\epsilon_d = 11$, calculated from series equivalent capacitance. Using effective permittivity is a valid approximation as the field confinement in the insulator is normal to the insulator interfaces, as we show in Sec. IV. In practice, a thin (~3 nm) Cr layer is sufficient to achieve the desired $I(V)$ characteristics.[14] A metal, such as Au, with better plasmonic properties can be added over the thin Cr to improve TWD rectenna performance. We performed a two-dimensional analysis in COMSOL of the TWD cross section, as shown in the inset of Fig. 1. The results show that the inclusion of the 3 nm layer of Cr has a small effect on plasmonic propagation characteristics compared to Au only. Specifically, without the Cr layer, the plasmonic decay length is $1.36\,\mu m$, and with a 3 nm layer of Cr, it is reduced to $1.31\,\mu m$, which is a reduction of less than 5%. In the model with no Au, the decay length is only 570 nm. Therefore, in this simulation, we ignore the thin Cr layer and make one lead of the TWD Au ($\epsilon_r = -2842\text{to}1339 * j$)[27] for enhanced plasmon propagation. The other TWD trace is Ni ($\epsilon_r = -1416\text{to}545 * j$).[27] We have ignored metal granularity in this model, which will likely degrade plasmonic propagation in any experimental device.

III. SOLVING FOR A NONLINEAR *I(V)* ELEMENT WITHIN A FINITE-ELEMENT SOLVER

Linear FEM solvers are unable to incorporate the nonlinear $I(V)$ characteristics of a diode. Therefore, TWD tunneling and rectification cannot be included in the EM simulation and must be incorporated during postprocessing. Without the inclusion of the diode $I(V)$ characteristics, the MIM insulator is modeled as perfectly insulating in the EM simulation. Therefore, the decay of the surface plasmon is solely the result of plasmonic resistive decay, i.e., resistive heating of the TWD. In reality, electron tunneling through the insulator also consumes power from the plasmonic wave and increases the rate of decay. This means that by ignoring the tunneling in the EM simulation, we are making an approximation that underestimates the total plasmonic decay. For this approximation to be valid, the total power taken from the plasmonic wave due to tunneling, P_{tunnel}, must be much smaller (<5%) than the plasmonic power, P_{spp}, the power that enters the TWD at the boundary between the TWD and antenna. In the case this condition is not met, the resulting fields from the EM simulation require modification during the postprocessing to reflect the additional decay due to tunneling.

Figure 2 illustrates the power flow through the rectenna system and where we make the distinction between the EM modeling and the postprocessing rectification calculation. First, in the EM portion of the simulation, a free-space wave is incident on the antenna. A portion of the incident power, P_{in}, is either transmitted or reflected, while the rest is absorbed, P_{abs}. Of the absorbed power, some is lost to resistive heating in the antenna; the rest is transmitted to the TWD, P_{spp}, based on the impedance match with the antenna. Of the power that is transmitted to the diode, some is lost to plasmonic resistive decay. The remainder drives both forward and reverse tunneling currents. This power flow, P_{tunnel}, is represented by a dashed arrow in Fig. 2 because it is excluded in the EM model due to the exclusion of tunneling. The net DC output, P_{dc}, is calculated from the net current due to the asymmetric electron tunneling in the MIM junction, also known as short-circuit current, I_{sc}. The difference between P_{tunnel} and the output power is the power lost to reverse leakage. In this paper, we will direct our analysis to finding the detectivity, D^*, which is a detector metric calculated using I_{sc}, shown in detail in Sec. VI.

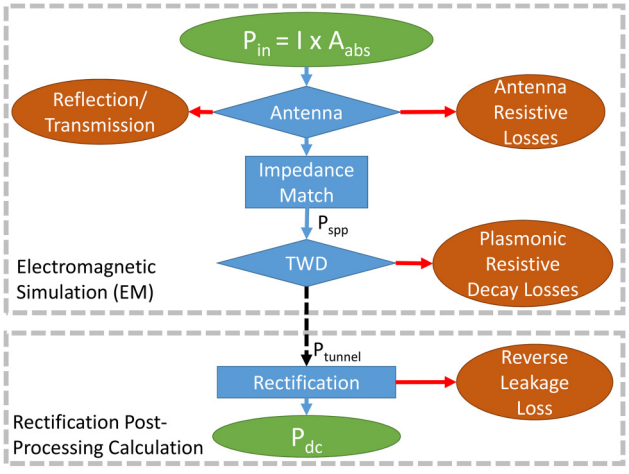

FIG. 2. Power flow in TWD operation and the separation of the EM simulation and postprocessing calculations. The total input power, P_{in}, is calculated from the product of radiation intensity and absorption area. Loss mechanisms include radiation not absorbed due to reflection or transmission past the antenna, resistive heating of the antenna and TWD, and electron tunneling in the reverse direction.

IV. TWD SURFACE PLASMON THEORY

A metal-insulator interface supports a confined electromagnetic mode, known as a surface plasmon polariton (SPP).[28,29] When two metal-insulator interfaces share a thin insulator, the SPPs on the two interfaces couple into either a symmetric mode or an antisymmetric mode. This coupling usually occurs when the separation between the two metal-insulator interfaces is less than 100 nm. Figure 3 shows the dispersion relationship for an Au-insulator-Au MIM structure calculated using the Drude model. We use the same effective insulator as in our TWD, $\epsilon_d = 11$ with a thickness of 5 nm. While the Ni-insulator-Au structure has slightly different dispersion characteristics due to the difference in metal dielectric constant values on either side of the insulator, the concepts remain the same and the Au-Insulator-Au configuration is a good approximation for the dispersion characteristics of our TWD structure. The dashed curve represents the single interface plasmon dispersion relationship. The single surface plasmon mode is confined to the area below the light-line and below the surface plasmon frequency, f_{spp},

$$f_{spp} = \frac{\omega_p}{2\pi\sqrt{1+\epsilon_d}}, \tag{4}$$

where ω_p is the plasma frequency of the metal. When two single surface modes couple, the symmetric and antisymmetric modes split from the single surface dispersion curve. The smaller the metal separation, the further the coupled modes move from the single surface. For a metal-to-metal separation much smaller than the wavelength, the symmetric mode exists above the surface plasmon frequency. The Coulomb repulsion prohibits SPP of the same charge to travel in phase without high energy, thus the symmetric mode dispersion is found at high frequency. This quasistatic treatment of the transverse field is generally valid for TEM transmission lines, assuming a negligible variation in the transverse fields. Therefore, one can say the "natural" mode of operation at low frequencies is the antisymmetric mode, which is equivalent to differential transmission line modes, hence the traveling-wave behavior of the surface plasmon. Given the smaller effective wavelength (larger k_z) for the plasmon relative to free-space, a transmission line that supports an antisymmetric SPP mode in the terahertz region is equivalent to what is known as a "slow-wave" transmission line in RF.

The symmetric and antisymmetric modes are depicted next to their respective dispersion curves. From the figure, it is clear that at 10.6 μm (~28 THz), only the antisymmetric mode is accessible. In this mode, there is a very large field confinement in the direction perpendicular to the insulator, E_x, as shown in Fig. 3, lower inset. This is crucial to the operation of a TWD, as it is this field that drives the electron tunneling through the asymmetric junction. The symmetric mode has an electric field null down the center of the insulator and cannot drive tunneling. Since the antisymmetric mode never intersects the light-line, it cannot be excited directly from a free-space wave, but rather require some sort of structure to achieve a momentum match.[30] In our case, the antenna fulfills this function.[31–33] The inclusion of the transition region, shown in Fig. 1, adds sharp curvature that allows charge concentration with alternating charges at smaller than the free-space wavelength periodicity, i.e., the larger k_z necessary for a momentum match.

V. EM SIMULATION RESULTS

We examine the field distribution at the center of the insulator and along the length of the TWD structure for an illuminated antenna to see what mode has been excited. Figure 4 shows the field strength in the insulator along the TWD length.

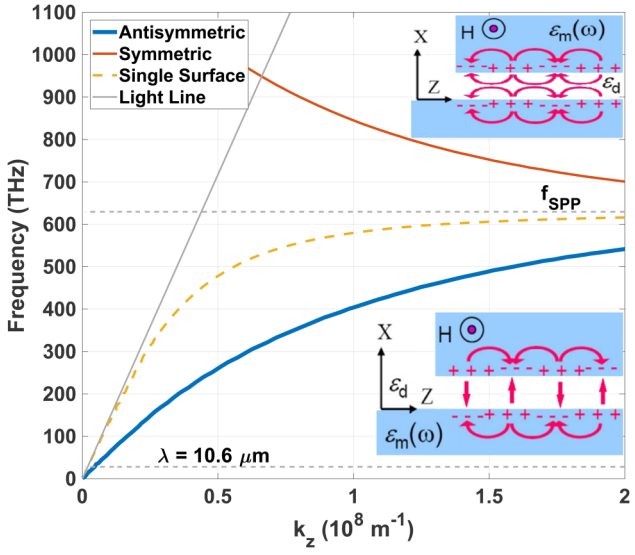

FIG. 3. Au-Insulator-Au dispersion characteristics for an MIM structure with a 5 nm insulator. The antisymmetric and symmetric mode field characteristics are illustrated next to their respective dispersion curves.

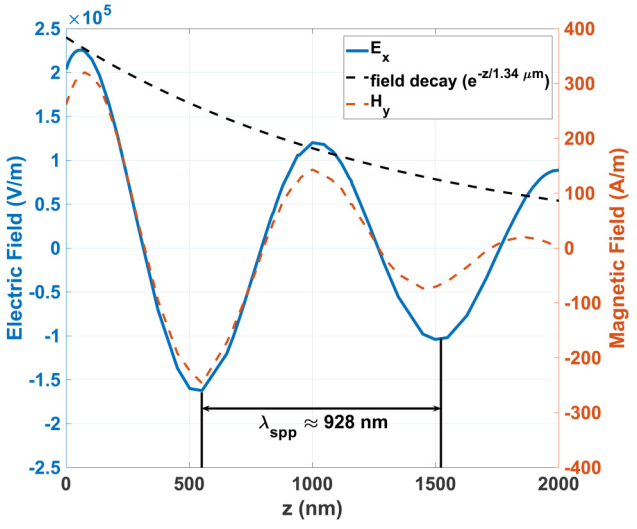

FIG. 4. Electric and magnetic fields (E_x and H_y) at the center of the MIM insulator along the length of the TWD (z-dimension) with the insulator thickness (t) of 5 nm, the metal thickness (t_m) of 120 nm, and the TWD length (L_{twd}) of 2.0 μm, for $I = 1 \times 10^5$ W/m^2 illumination condition.

The alternating polarity of E_x confirms the excitation of the antisymmetric mode described in Sec. IV. At the beginning of the TWD, $z = 0$, E_x starts in phase with H_y showing that power is propagating in the positive z-direction. Only at the end of the TWD, we see a shift in the relative phases of E_x and H_y due to reflections at the open transmission line termination. The reflection off the end of the TWD also explains why the field exceeds the expected decay envelope, represented by the dashed black line in Fig. 4. We can see that the plasmonic wavelength, λ_{spp}, is ~928 nm and the decay length, ℓ, is ~1.34 μm. A larger ℓ is desirable as it indicates less resistive plasmonic decay loss.

Table I summarizes the plasmonic wavelength, λ_{spp}, and decay length, ℓ, for the four TWD cross sections considered. This table shows us that as t_m is reduced both ℓ and λ_{spp} increase. As t is reduced, both ℓ and λ_{spp} decrease too.

We can calculate the total power absorbed in the rectenna, P_{abs}, as the sum of the antenna resistive loss, the plasmonic resistive decay loss, the reverse leakage loss, and the rectified output. In addition to the xz upper boundary port where the plane-wave is excited, there is a second xz boundary port, port 2, on the bottom of the silicon substrate. This port calculates the through power, that is, the power that is transmitted past the device and through the substrate. Given that air, SiO_2, and Si are all nearly lossless at 10.6 μm,[27] the power absorbed in the rectenna can be approximated as the total power absorbed in the system. The total power absorbed in the system is the difference between the input power to the system and the sum of the power that exits the upper and lower ports,

$$P_{abs} = IA_{p1}(1 - |S_{11}|^2 - |S_{21}|^2), \tag{5}$$

where I is the input intensity, A_{p1} is the area of port 1, and S_{11} and S_{21} are the S-parameters for ports 1 and 2, respectively.

Length has an important effect on the total absorbed power, as Fig. 5 shows. We see that the length of the TWD can establish a resonant behavior. These resonant peaks occur at ~$\lambda_{spp}/2$ intervals. The size of the resonant peaks decreases for longer TWDs. Additionally, the height of the resonant peaks decreases faster for increased length when the cross-sectional geometry has a shorter decay length, as is the case for the 2.5 nm insulator. From an impedance perspective, narrow transmission lines, which corresponds to smaller t_m, result in a better coupling efficiency to the antenna. This is due to the capacitive nature of the antenna impedance. Perfectly matched source and load impedances are complex conjugates of each other. With a narrower TWD, the input impedance becomes more inductive, and, therefore, a better match to the antenna. We observe a similar effect with insulator thickness, as t increases, the TWD capacitance is reduced, and the match is improved. As the TWD becomes substantially longer than the decay length, the variations in impedance with length decrease as the antenna no longer sees the open circuit termination of the line.

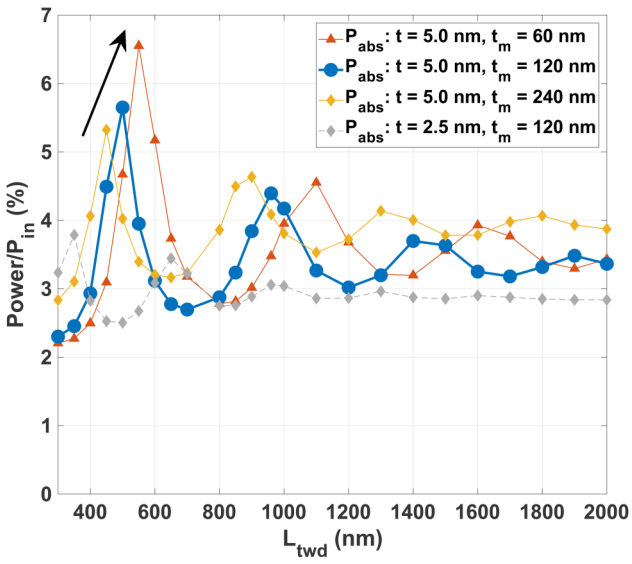

FIG. 5. Fraction of the incident illumination power that is absorbed in the TWD rectenna vs TWD length for different cross-sectional geometries (insulator and metal thicknesses).

To confirm that the resonance behavior we see in Fig. 5 is due to impedance match, we model the antenna and the diode separately. We excite each structure at the interface where they meet, illustrated by the TWD cross section in Fig. 1, using a lumped-port voltage excitation. The voltage is applied from the Ni (M1) to the Au (M2) across the TWD insulator. This allows us to estimate the impedance of the two individual elements so we can calculate the coupling efficiency. Of the three TWD dimensions we vary, the two cross-section dimensions affect the antenna: t_m and t. While we keep the antenna geometry mostly constant, we make the small changes necessary to prevent sharp steps at the transition boundary between the antenna and TWD. The antenna impedance for the four sets of TWD cross-section dimensions is summarized in Table II.

TABLE I. TWD plasmonic wavelength and decay length.

Insulator thickness (t)	Metal thickness (t_m) 60 nm	120 nm	240 nm
t = 2.5 nm	Not simulated	ℓ = 760 nm λ_{spp} = 631 nm	Not simulated
t = 5.0 nm	ℓ = 1.42 μm λ_{spp} = 1.06	ℓ = 1.34 μm λ_{spp} = 928 nm	ℓ = 1.26 μm λ_{spp} = 850 nm

TABLE II. Antenna impedance.

Insulator thickness (t)	Metal thickness (t_m) 60 nm	120 nm	240 nm
t = 2.5 nm	Not simulated	61–95j Ω	Not simulated
t = 5.0 nm	117–112j Ω	80–104j Ω	45–82j Ω

From the decoupled TWD simulation, the real part of TWD input impedance for our geometries varies from 6 to 95 Ω and the imaginary part varies from −8 to 63 Ω. This variation comes largely from the TWD length dependence. Using the antenna and TWD impedances, the coupling efficiency is calculated using the following equation:

$$\eta_c = \frac{4R_{twd}R_{ant}}{(R_{twd}+R_{ant})^2+(X_{twd}+X_{ant})^2}, \tag{6}$$

where R_{ant} and X_{ant} represent the real and imaginary parts of the antenna impedance, respectively. R_{twd} and X_{twd} are the real and imaginary parts of the TWD input impedance, respectively, not to be confused with the diode DC resistance calculated by (14) and used in (13) and (15). The resulting coupling efficiency from (6) is plotted in Fig. 6 vs TWD length for the cross-section variations of interest.

While the impedance coupling efficiency results are informative and show what sort of effect we should expect from TWD geometry variations, they are more qualitative than quantitative due to the method of excitation. Comparing Figs. 5 and 6, the geometry effects are much more pronounced in the decoupled impedance match calculation (Fig. 6). Figures 7(a) and 7(b) show the surface currents at the cross-sectional boundary between the antenna and TWD, illustrated in Fig. 1, from the decoupled antenna and TWD simulations, respectively. These modes look very similar as both were excited by applying a potential difference at the inner edges of the diode metals. In both cases, the modes are contained tightly around the diode insulator gap, where the excitation occurred. Figure 7(c) shows the coupled antenna/TWD simulation and the surface currents on the antenna/TWD interface are much more distributed. This is because in the coupled model, the entire rectenna is excited by a 10.6 μm plane-wave. In this case, all the surfaces of the metal in the transition region, not just the surfaces at the MIM junction, are used to carry current as the antenna concentrates the plasmonic energy to the feed-point and the MIM insulator. Because of the more concentrated current in the decoupled simulations, Fig. 6, compared to Fig. 5, exaggerates the effect of changes in geometry on the calculated impedance match.

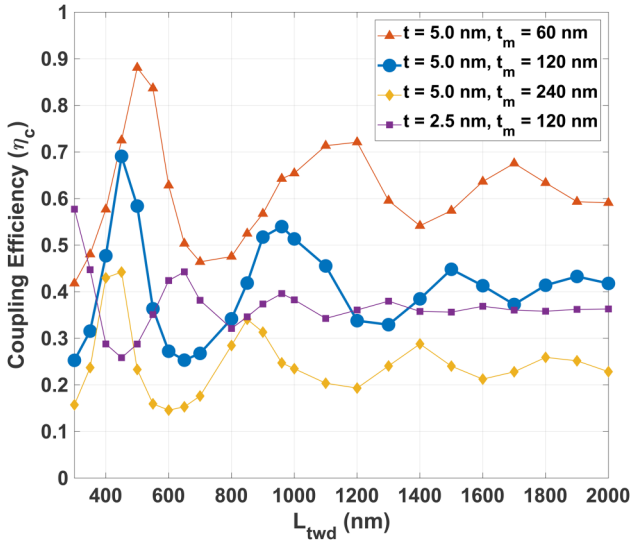

FIG. 6. Decoupled calculated impedance match efficiency for different TWD geometries vs length of the TWD.

VI. POST PROCESSING AND RECTIFICATION PERFORMANCE

The MIM asymmetric tunneling characteristics are added in postprocessing using the $I(V)$ equation generated by (2) from Ref. 23 to calculate the tunneling currents. We use a TWD rectenna without an external DC bias, as it has an experimental advantage of avoiding possible bolometric effects in a measurement. Since we have a TWD, the MIM junction does not have the same voltage everywhere. Therefore, we must use the DC $I(V)$ characteristics of the diode and the modeled electric field to calculate the current through the insulator. Given the relative uncertainty of the insulator thickness from the measured MIM diode, we want the tunneling estimate in the postprocessing calculation to be dependent on the area of the simulated TWD but independent of the insulator thickness chosen in the EM simulation. Therefore, we define a voltage dependent conductance per unit area, G_a(V), rather than a conductivity. To convert $I(V)$ to G_a(V), we use the following:

$$G_a(V) = \frac{I(V)}{VL_{twd}t_m}, \tag{7}$$

where L_{twd} is 3 μm and t_m is 115 nm for the experimental device on which the $I(V)$ characteristic is based. Before proceeding to analyze the rectification performance of the TWD rectenna with metrics like detectiviy and short-circuit current, we need to check that our assumptions are valid; specifically, that P_{tunnel} is much less than P_{spp} (<5%). The plasmonic power, P_{spp}, is the power that enters the TWD in the form of a surface plasmon at the boundary between the diode and the antenna. The amount of power transferred is determined by the impedance match. It is calculated using the Poynting vector integrated over the cross-sectional area of the diode insulator in the plane normal to the propagation direction,

$$P_{spp} = \frac{1}{2}\int_0^t\int_0^{t_m} Re(\overline{E}_x \times \overline{H}_y^*)\cdot\hat{z}\,dx\,dy. \tag{8}$$

Given the current distribution in Fig. 7(c), this calculation tends to understate P_{spp} as it only includes the power on the MIM interface. To calculate P_{tunnel}, we take the average over a full 2π cycle of incident radiation of the tunneling power density (voltage times current density) integrated over the yz cut-plane at the center of the MIM insulator,

$$P_{tunnel} = \int_0^{2\pi}\int_0^{L_{twd}}\int_0^{t_m} \frac{G_a(E_x t)E_x^2 t^2}{2\pi}\,dy\,dz\,d\phi, \tag{9}$$

where E_x is the electrical field in the x-direction, normal to the MIM interface, and is a function of position (y and z), and phase of the illumination wave, ϕ. From evaluating (8) and (9), at a maximum, P_{tunnel} is 3.9% of the P_{spp}. Therefore, the additional

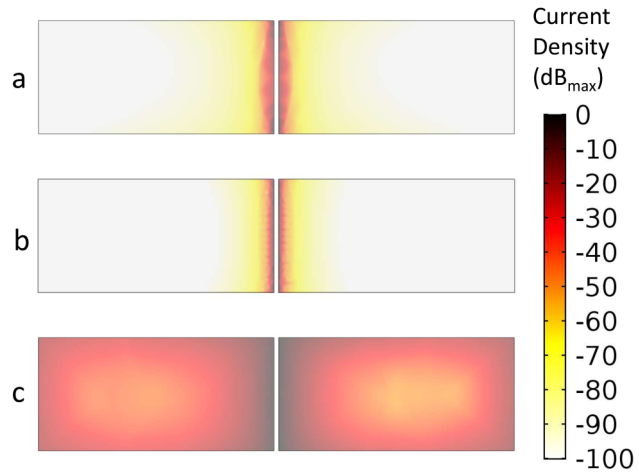

FIG. 7. Surface current at the cross-sectional boundary at the TWD/antenna interface. Normalized current density in decibels for (a) antenna only simulation, (b) TWD only simulation, and (c) coupled simulation.

plasmonic decay due to tunneling can be ignored. Now that we have confirmed the validity of our initial assumptions, we can calculate the final performance metrics such as short-circuit current and detectivity. The first metric to calculate is short-circuit current with an equation very similar to (9) for P_{tunnel}. We integrate the current density over the insulator area and average over a full 2π cycle of incident radiation,

$$I_{sc} = \int_0^{2\pi}\int_0^{L_{twd}}\int_0^{t_m} \frac{G_a(E_x t)E_x t}{2\pi}\, dy\, dz\, d\phi. \tag{10}$$

Using short-circuit current, system responsivity can be calculated as

$$\beta_{sys} = \frac{I_{sc}}{P_{in}}. \tag{11}$$

System responsivity is the ratio of DC current and optical AC input power. From system responsivity, we calculate specific detectivity,[34]

$$D^* = \sqrt{A_{abs}\Delta f}\frac{\beta_{sys}}{I_n}, \tag{12}$$

where Δf is the detector bandwidth, A_{abs} is the rectenna absorption area, and I_n is the noise current calculated in (13) from the Johnson noise due to the diode resistance and the shot noise due to DC bias,

$$I_n = \sqrt{\Delta f\left(2qI_{bias} + \frac{4kT}{R_0}\right)}. \tag{13}$$

In (13), k is the Boltzmann constant, q is the electron charge, and T is the temperature, taken to be 300 K for this work. I_{bias} is the DC bias current, taken to be zero for this work as we have modeled an asymmetric MIM designed to operate at zero-bias. The zero-bias diode resistance, R_0, is calculated from (7) evaluated at $V = 0$ as

$$R_0 = (G_a(0)L_{twd}t_m)^{-1}. \tag{14}$$

The detectivity from (12) can be simplified by combining (12) and (13). The detector bandwidth terms cancel and leaves the following:

$$D^* = \beta_{sys}\sqrt{A_{Abs}}\sqrt{\frac{R_0}{4kT}}. \tag{15}$$

Figure 8 shows detectivity vs length of various TWDs and a lumped-element rectenna with the equivalent MIM area and junction characteristics as the TWD with $t = 5$ nm, $t_m = 120$ nm, for any given length. For the lumped-element (LE) diode, short-circuit current was calculated with the following:

$$I_{sc/LE} = P_{in}\eta_{ant}\eta_c\beta_0, \tag{16}$$

where η_{ant} is the maximum antenna absorption given in Sec. II, ~13%, and β_0 is the zero-bias responsivity, 0.49 A/W, calculated from the DC $I(V)$ fit[23] summarized in Sec. II. The coupling efficiency, η_c, comes from (6), where the TWD impedance is replaced with the series equivalent of the diode resistance in parallel with the diode capacitance ($R_0 \| 1/j\omega C_d$). The capacitance of the diode, C_d, is calculated as the planar geometric capacitance.[26] As expected, the lumped-element and the equivalent TWD detectivities converge for extremely short TWDs. For the thin (2.5 nm) insulator TWD, the detectivity is substantially lower than the TWDs with 5.0 nm insulators. In Sec. II, we noted that we used the same $I(V)$ characteristics for both insulator thicknesses. From Fig. 6, we know that the 2.5 nm insulator has similar coupling efficiency to the 5.0 nm insulator. Because of the identical $I(V)$

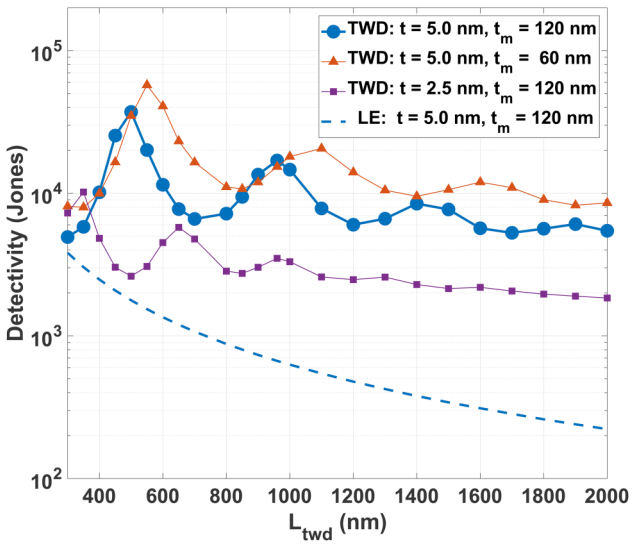

FIG. 8. TWD detectivity vs TWD length for varying TWD cross sections and a comparison lumped-element (LE) rectenna.

characteristics and similar coupling efficiencies, we can conclude that the lower detectivity of the thinner insulator is primarily a result of the shorter plasmon propagation length.

For the two variations of the 5 nm insulator shown, the detectivies exhibit the same trend established by the diode impedance match in Fig. 6.

We compare the TWD in this work that has dimensions that are closest to the dimensions of the TWD cross section from the 2D model used by Grover *et al.*[15] Grover *et al.* used a 2D model with $t = 2.0\,\text{nm}$, $t_m = 100\,\text{nm}$ and assumed L_{twd} to be greater than decay length. The most representative device from this work is the TWD with $t = 2.5\,\text{nm}$, $t_m = 120\,\text{nm}$, and $L_{twd} = 2000\,\text{nm}$. The detectivity reported in Fig. 8 is lower by a factor of ~1600; Grover reported 3×10^6 Jones at $10.6\,\mu\text{m}$, and we observed 1.85×10^3 Jones. This difference stems from three fundamental expansions in this paper. First, Grover assumes a perfectly efficient antenna, while our maximum absorption is ~13% due to the illumination from the low-index side of the antenna. Second, Grover also assumes perfect impedance match, while our coupling efficiency is calculated explicitly, simulated directly, and found to be ~22% (out of the maximum ~13% absorption for our antenna, 2.8% was observed in Fig. 5). Finally, Grover uses a biased responsivity from a simulated $I(V)$ curve that we estimate to be 14 times larger than the zero-bias responsivity we use with our unbiased detector. Additionally, using (13), we estimate our noise current to be 5.5 pA. From (12), we can estimate Grover's noise current to be 3.3 pA, a factor of ~1.7 times lower than ours. Table III summarizes the estimated effects of these differences.

The combined effects of the assumptions made by Grover *et al.* result in an increase in detectivity and system responsivity by a factor of ~860, which is the product of all four improvement factors in Table III: 8, 4.5, 14, and 1.7. The additional factor of ~2 could be due to any combination of a number of effects, including slight variations in cross section, and different materials. Considering Grover *et al.*'s idealistic assumptions, our results are consistent with Grover's predictions.

Using the design techniques in this paper, we observed a ~31× increase in detectivity, from 1.85×10^3 to 5.75×10^4 Jones, from a device with a thicker insulator, narrower overlap, and shorter length ($t = 5.0\,\text{nm}$, $t_m = 60\,\text{nm}$, $L_{twd} = 550\,\text{nm}$) (instead of $t = 2.5\,\text{nm}$, $t_m = 120\,\text{nm}$, $L_{twd} = 2000\,\text{nm}$ that was most representative of Grover *et al.* TWD). This improvement derives from four improvements: First, the improved coupling efficiency accounts for a factor of ~2.3 based on the higher absorption in Fig. 5 (2.8% increased to 6.5%). Second, the reduced area ($2000 \times 120\,\text{nm}^2$ decreased to $550 \times 60\,\text{nm}^2$) leads to a proportionality higher resistance. From (15), detectivity scales as the square root of resistance for a detectivity increase by a factor of ~2.7. Third, the thicker insulator and narrower overlap lead to a longer decay length from Table I. We can estimate the improvement in detectivity due to increased decay length from Figs. 5 and 8. For the change in TWD cross section, holding the length constant at 2000 nm, the detectivity increases by a factor of 4.64 (1.85×10^3 Jones to 8.56×10^3 Jones). This increase is due to the product of the improved coupling efficiency and the longer decay length. The same comparison for absorption yields a factor of ~1.2 (2.84%–3.4%), which is due to the improved coupling efficiency only and is unaffected by the increased decay length. Therefore, we estimate the improvement due to increased decay length to be ~3.9 (4.64/1.2; the improvement due to both better impedance matching and longer decay length divided by the improvement due to impedance matching only). These first three factors, summarized in Table IV, multiply for an overall improvement by a factor of ~24 (the product of the first three improvement factors: 2.3, 2.7, and 3.9). The final improvement of ~1.3 is the result of higher electric field due to reflections at the open termination of the TWD. When the device length is shortened, more power is reflected. This increased refection leads to a higher field and larger voltage swings on the $I(V)$ curve and better rectification. Thus, we examine how to design a TWD with coupling characteristics near Grover's idealistic assumptions.

Table IV contains TWD coupling efficiencies ranging from 22% to 50%. If we calculated the best lumped-element coupling efficiency in Fig. 8, using the method described in Sec. VI, we get 0.034%. This is in an improvement of more than three orders of magnitude.

TABLE III. Sources of discrepancy between simulations (Grover *et al.* vs this work).

Source of discrepancy	Grover *et al.*	TWD—(similar to Grover *et al.*) $t = 2.5\,\text{nm}$ $t_m = 120\,\text{nm}$ $L_{twd} = 2000\,\text{nm}$	Detectivity improvement factor
Antenna efficiency (η_a)	100%	13%	8
Coupling efficiency (η_c)	100%	22%	4.5
Diode responsivity (β_0)	~7 A/W	0.49 A/W	14
Noise current (I_n)	3.3 pA	5.5 pA	1.7

TABLE IV. Improvement factors.

Source of improvement	TWD—(similar to Grover *et al.*) $t = 5.0\,\text{nm}$ $t_m = 120\,\text{nm}$ $L_{twd} = 2000\,\text{nm}$	Best TWD $t = 5.0\,\text{nm}$ $t_m = 60\,\text{nm}$ $L_{twd} = 550\,\text{nm}$	Detectivity improvement factor
Coupling efficiency (η_c)	22%	50%	2.3
Diode area	$2000 \times 120\,\text{nm}^2$	$550 \times 60\,\text{nm}^2$	2.7
Decay length (ℓ)	760 nm	$1.42\,\mu\text{m}$	3.9

VII. CONCLUSION

We have presented a comprehensive analysis of the interaction between the antenna and the TWD. The analysis has taken into account the nonlinear transmission line loading as a first order approximation. We showed that such an approximation is valid for low tunneling currents. We use this method to study the effects of TWD cross-section dimensions and TWD length. At lengths greater than the decay length of the surface plasmon, the effect of length is

minimal. However, when the length is shortened to less than a decay length, resonant peaks that appear as a function of length become very pronounced. When the TWD input impedance is well matched to the antenna impedance, we see resonance peaks that improve the overall operation of the rectenna. The TWD improves the coupling efficiency between the antenna and diode by more than three orders of magnitude compared to the lumped-element. However, not all of that improvement is realized in detectivity, where we only see an improvement of about one order of magnitude in Fig. 8. This is because the TWD has an additional loss mechanism: the plasmonic propagation down the MIM interface. Despite the plasmonic loss limiting the overall improvement, this TWD study demonstrates that a carefully designed rectenna system can overcome fundamental limitations such as RC time constant.

SUPPLEMENTARY MATERIAL

See the supplementary material for additional information on MIM tunneling, diode $I(V)$ characteristics, and field confinement in the transition region between the TWD and antenna.

ACKNOWLEDGMENTS

The authors would like to thank Wounjhang Park, Ayendra Weerakkody, Amina Belkadi, and John Stearns for their helpful discussions. G. Moddel holds stock in RedWave Energy, Inc. The work presented herein was funded, in part, by the Advanced Research Projects Agency-Energy (ARPA-E), U.S. Department of Energy, under Award No. DE-AR0000676, in collaboration with RedWave Energy, Inc.

REFERENCES

[1]H. Neil *et al.*, "Microwave to dc converter," U.S. patent 3,434,678 (March 1969).
[2]W. C. Brown, "The history of the development of the rectenna," in NASA. Johnson Space Center Solar Power Satellite Microwave Transmission and Reception, 271–280 (1980).
[3]R. L. Bailey, "A proposed new concept for a solar-energy converter," J. Eng. Power **94**, 73–77 (1972).
[4]J. Zhang and Y. Huang, "Rectennas for wireless energy harvesting," dissertation (University of Liverpool, 2013).
[5]T. E. Hartman, "Tunneling of a wave packet," J. Appl. Phys. **33**, 3427–3433 (1962).
[6]M. Heiblum, S. Wang, J. Whinnery, and T. Gustafson, "Characteristics of integrated MOM junctions at dc and at optical frequencies," IEEE J. Quantum Electron. **14**, 159–169 (1978).
[7]B. J. Eliasson, "Metal-insulator-metal diodes for solar energy conversion," Ph.D. thesis (University of Colorado, 2001).
[8]N. M. Miskovsky, P. H. Cutler, A. Mayer, B. L. Weiss, B. Willis, T. E. Sullivan, and P. B. Lerner, "Nanoscale devices for rectification of high frequency radiation from the infrared through the visible: A new approach," J. Nanotechnol. **2012**, 1 (2012).
[9]M. Nagae, "Response time of metal-insulator-metal tunnel junctions," Jpn. J. Appl. Phys. **11**, 1611 (1972).
[10]S. Grover and G. Moddel, "Applicability of metal/insulator/metal (MIM) diodes to solar rectennas," IEEE J. Photovoltaics **1**, 78–83 (2011).
[11]A. Sanchez, C. Davis, Jr., K. Liu, and A. Javan, "The MOM tunneling diode: Theoretical estimate of its performance at microwave and infrared frequencies," J. Appl. Phys. **49**, 5270–5277 (1978).
[12]M. J. Estes and G. Moddel, "Surface plasmon devices," U.S. patent 7,010,183 (7 March 2006).
[13]P. C. Hobbs, R. B. Laibowitz, F. R. Libsch, N. C. LaBianca, and P. P. Chiniwalla, "Efficient waveguide-integrated tunnel junction detectors at 1.6 μm," Opt. Express **15**, 16376–16389 (2007).
[14]B. Pelz, A. Belkadi, and G. Moddel, "Traveling-wave metal-insulator-metal diodes for infrared rectennas," in *IEEE Photovoltaic Specialist Conference* (IEEE, 2016).
[15]S. Grover, O. Dmitriyeva, M. J. Estes, and G. Moddel, "Traveling-wave metal/insulator/metal diodes for improved infrared bandwidth and efficiency of antenna-coupled rectifiers," IEEE Trans. Nanotechnol. **9**, 716–722 (2010).
[16]I. E. Hashem, N. H. Rafat, and E. A. Soliman, "Dipole nantennas terminated by traveling wave rectifiers for ambient thermal energy harvesting," IEEE Trans. Nanotechnol. **13**, 767–778 (2014).
[17]I. E. H. Sayed, N. H. Rafat, and E. A. Soliman, "Harvesting thermal infrared emission using nanodipole terminated by traveling wave rectifier," in *2015 9th European Conference on Antennas and Propagation (EuCAP)* (IEEE, 2015), pp. 1–5.
[18]X. Lei and V. Van, "FDTD modeling of traveling-wave MIM diode for ultrafast pulse detection," Opt. Commun. **294**, 344–350 (2013).
[19]S. Grover and G. Moddel, "Engineering the current–voltage characteristics of metal–insulator–metal diodes using double-insulator tunnel barriers," Solid State Electron. **67**, 94–99 (2012).
[20]P. Maraghechi, A. Foroughi-Abari, K. Cadien, and A. Elezzabi, "Enhanced rectifying response from metal-insulator-insulator-metal junctions," Appl. Phys. Lett. **99**, 253503 (2011).
[21]N. Alimardani, J. M. McGlone, J. F. Wager, and J. F. Conley, Jr., "Conduction processes in metal–insulator–metal diodes with Ta_2O_5 and Nb_2O_5 insulators deposited by atomic layer deposition," J. Vac. Sci. Technol. A **32**, 01A122 (2014).
[22]D. A. D. Chathuranga, "Engineered high-k oxides," Ph.D. thesis (University of Liverpool, 2016).
[23]B. Pelz, A. Belkadi, and G. Moddel, "Avoiding erroneous analysis of MIM diode current-voltage characteristics: Exponential fitting," Measurement **120**, 28–33 (2018).
[24]D. Rutledge and M. Muha, "Imaging antenna arrays," IEEE Trans. Antennas Propag. **30**, 535–540 (1982).
[25]Z. Thacker and P. J. Pinhero, "Terahertz spectroscopy of candidate oxides in MIM diodes for terahertz detection," IEEE Trans. Terahertz Sci. Technol. **6**, 414–419 (2016).
[26]A. Belkadi, A. Weerakkody, and G. Moddel, "Large errors from assuming equivalent dc and high-frequency electrical characteristics in metal–multiple-insulator–metal diodes," ACS Photonics **5**, 4776–4780 (2018).
[27]E. D. Palik, *Handbook of Optical Constants of Solids* (Academic Press, 1998), Vol. 3.
[28]D. Woolf, M. Loncar, and F. Capasso, "The forces from coupled surface plasmon polaritons in planar waveguides," Opt. Express **17**, 19996–20011 (2009).
[29]M. Fox, "Optical properties of solids," Am. J. Phys. **70**, 1269 (2002).
[30]A. H. Nicol, "Grating coupled surface plasmon enhanced fluorescence spectroscopy," Dizertační práce (univerzita Mainz, 2005).
[31]P. Muehlschlegel, H.-J. Eisler, O. J. Martin, B. Hecht, and D. Pohl, "Resonant optical antennas," Science **308**, 1607–1609 (2005).
[32]M. W. Knight, H. Sobhani, P. Nordlander, and N. J. Halas, "Photodetection with active optical antennas," Science **332**, 702–704 (2011).
[33]L. Novotny and N. Van Hulst, "Antennas for light," Nat. Photonics **5**, 83–90 (2011).
[34]A. Rogalski, "Infrared detectors: Status and trends," Prog. Quantum Electron. **27**, 59–210 (2003).